

# Distributed Acoustic Sensing for aftershock monitoring: the case of the 2019 $M_w$ 4.9 Le Teil earthquake

**Martijn van den Ende**  \*<sup>1</sup>, **Jean-Paul Ampuero**  <sup>1</sup>, **Françoise Courboulex**  <sup>1</sup>, **Bertrand Delouis**  <sup>1</sup>, **Maxime Godano**  <sup>1</sup>, **Christophe Larroque**  <sup>1,2</sup>, **Anthony Sladen**  <sup>1</sup>

<sup>1</sup>Université Côte d'Azur, CNRS, IRD, Observatoire de la Côte d'Azur, Géoazur, France, <sup>2</sup>Université de Reims Champagne-Ardenne, GEGENAA, Reims, France

## Contents:

- Figure S1: Tectonic context of the Le Teil epicentral region
- Figure S2: DAS recordings of three selected aftershocks
- Figure S3: Comparison of velocity models
- Table S4: Seismic station metadata and phase picks (available in CSV format)

---

\*Corresponding author: martijn.vandenende@oca.eu

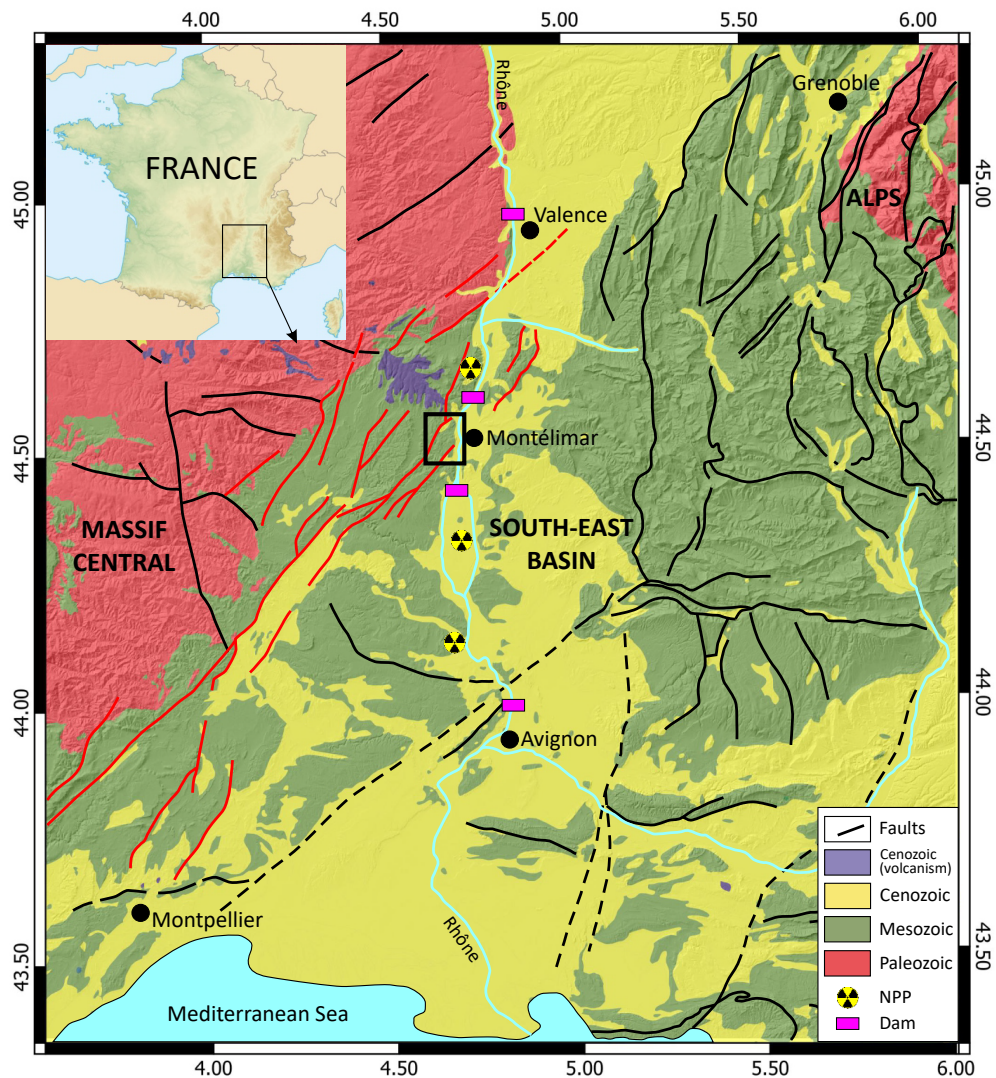


**Figure S1** Tectonic setting of the Le Teil epicentral region. The area of study is positioned within the black box near the centre of the figure (west of Montélimar). Also indicated are nuclear powerplants (NPP) and major dams along the Rhône river.

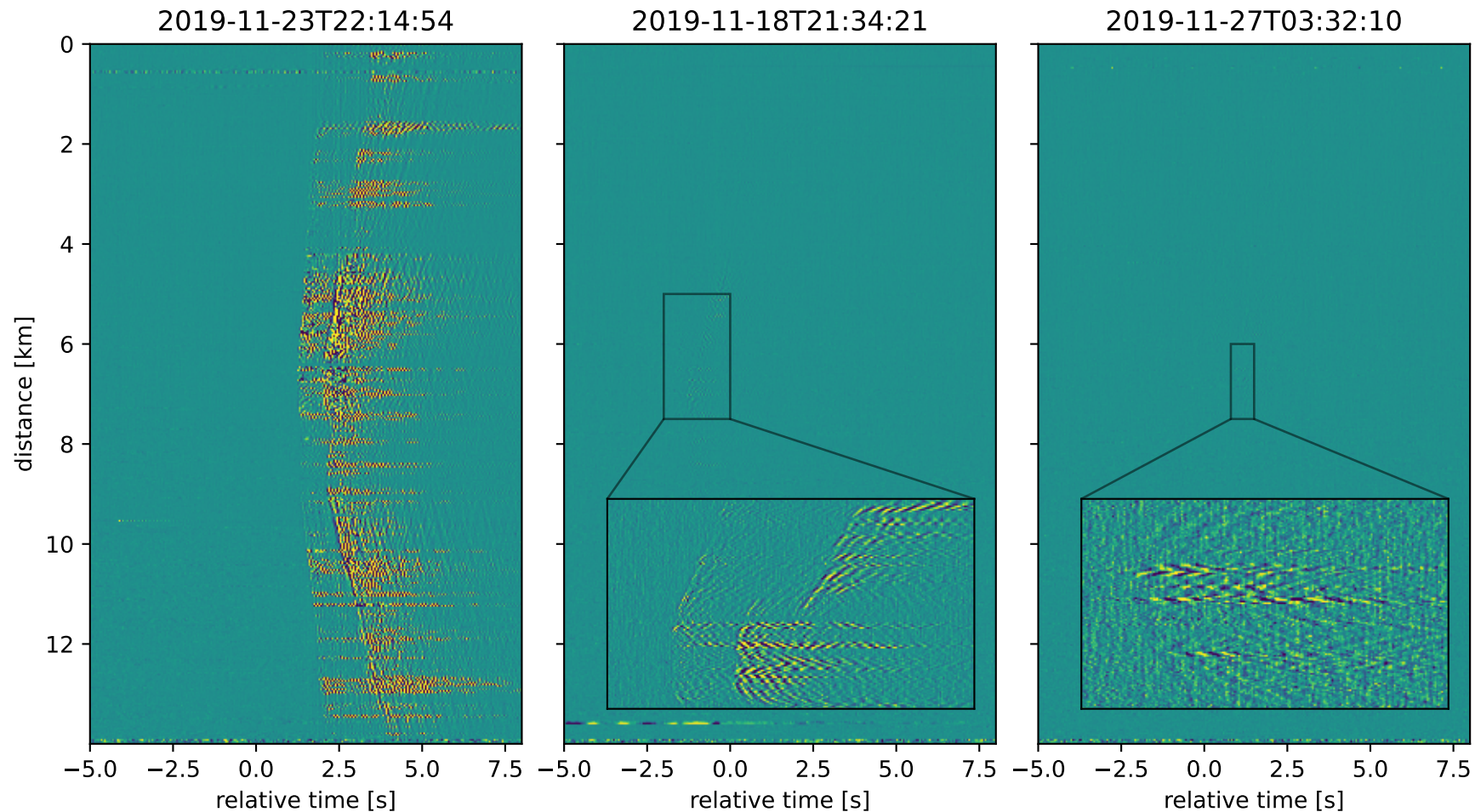


**Figure S2** DAS recordings of three selected aftershocks with largest estimated magnitudes, in descending order of signal-to-noise ratio. While the principal aftershock has a reasonable SNR over most of the cable, the signal amplitudes of the other two events barely exceed the noise level. Each of the three main panels has the same colour range, but the colour range of the insets is adjusted to highlight the details of each event. The origin time of each event is as indicated above each panel.

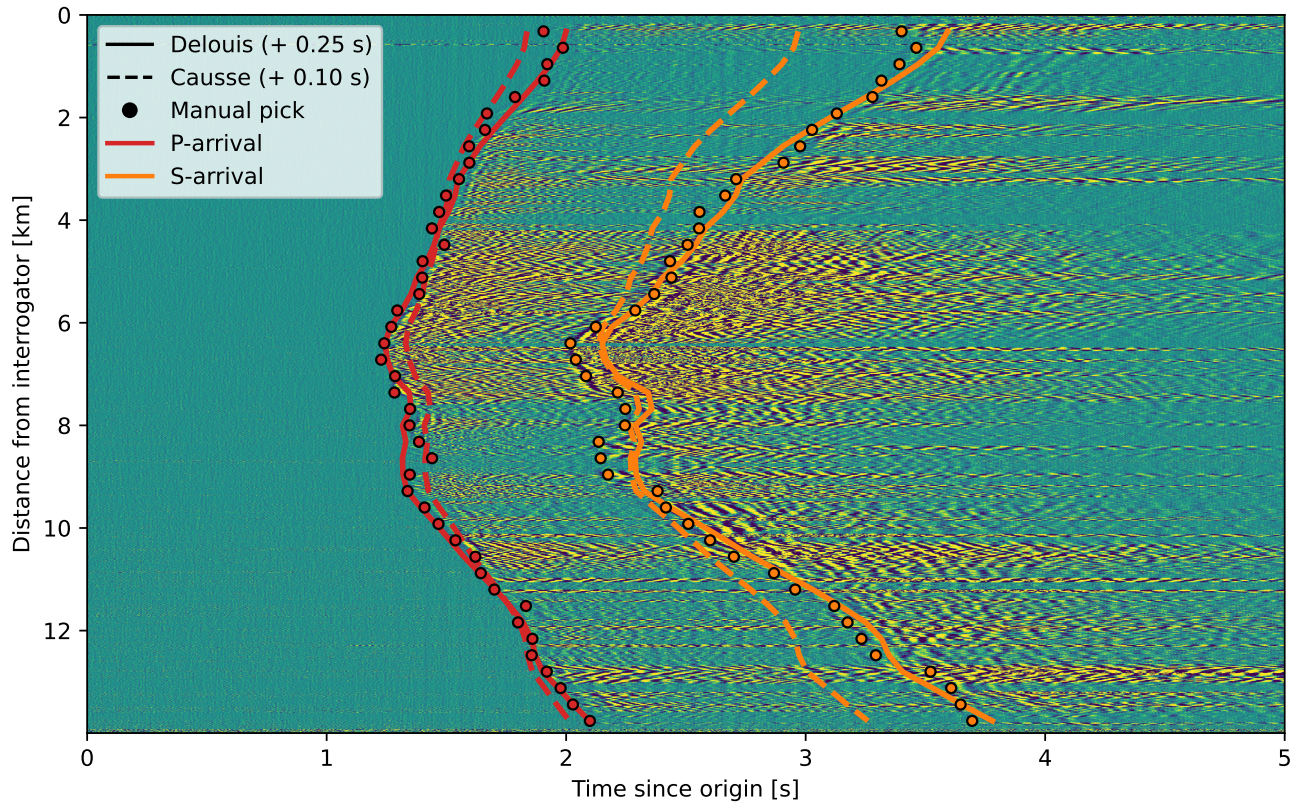


**Figure S3** Comparison of two proposed velocity models with DAS recordings. Manual picks of the first P- and S-phase arrivals were made every 100 channels (solid disks). The corresponding arrival times predicted for the constant-gradient model proposed by [Delouis et al. \(2022\)](#), and the layered model proposed by [Causse et al. \(2021\)](#) are indicated by the solid and dashed lines, respectively. For each velocity model, the corresponding hypocentre location and origin time were used (i.e., which were inverted assuming each given velocity model). The optimal fit with the observed P-arrivals is obtained by shifting the origin time by +0.25 s for the model of [Delouis et al. \(2022\)](#), and by +0.10 s for that of [Causse et al. \(2021\)](#). The largest discrepancy between the two velocity models is seen for the S-arrivals; it is apparent that the velocity model of [Causse et al. \(2021\)](#) exhibits an average S-wave speed that is too low. The velocity model of [Delouis et al. \(2022\)](#) overall has a satisfactory fit, motivating our choice for this velocity model for the SVI inversion.

Station code	Latitude [°]	Longitude [°]	Elevation [m]	P-pick	S-pick
ALBA	44.554879	4.603087	220	1.02	2.39
AUBI	44.5769	4.62346	326	1.16	2.68
BEAU	44.500019	4.627541	150	0.594	1.489
CAMP	44.4892	4.6766	116	0.41	1.06
CROT	44.50289	4.626209	115	0.594	1.453
ILES	44.52557	4.71973	75	0.5	1.409
LAFA	44.5137	4.6636	273	0.084	0.468
LARN	44.44704	4.59211	310	1.877	3.864
MONN	44.5838	4.7499	70	1.567	3.32
N01	44.497517	4.653054	105	0.373	0.961
N02	44.522556	4.620619	157	0.593	1.571
N03	44.519306	4.646326	328	0.233	0.8
N04	44.522254	4.654546	266	0.151	0.593
N05	44.54181	4.65486	155	0.332	0.952
N06	44.549888	4.631562	217	0.699	1.64
N07	44.52917	4.664568	185	0.064	0.368
N08	44.512191	4.685316	68	0.08	0.42
N09	44.513403	4.653802	186	0.171	0.622
N10	44.515146	4.663737	91	0.06	0.452
N11	44.511593	4.634662	270	0.409	-
N12	44.512454	4.635169	273	0.405	1.102
N13	44.512364	4.634686	265	0.405	1.101
N14	44.511675	4.635292	270	0.405	1.1
N15	44.512089	4.634934	272	0.405	1.1
N16	44.487922	4.61879	122	0.85	1.927
N17	44.482045	4.690227	71	0.542	1.363
N18	44.558621	4.61742	300	0.942	2.27
N19	44.481999	4.690224	71	0.54	1.374
N20	44.482053	4.690195	71	0.537	1.463
N21	44.548453	4.632406	205	0.668	1.657
N22	44.548459	4.630398	199	0.687	1.666
N23	44.55187	4.632665	225	0.714	1.69
N24	44.550611	4.631682	215	0.71	1.713
N25	44.512164	4.685332	68	0.081	0.55
N26	44.513731	4.643173	279	0.285	0.898
N27	44.511956	4.685299	68	0.086	0.563
N28	44.482041	4.690065	71	0.54	1.344
STIL	44.52256	4.62061	155	0.593	1.55
TEIL	44.550396	4.683843	70	0.449	1.166
THOC	44.502632	4.622869	147	0.65	1.549
THOM	44.500429	4.626154	231	0.613	1.508
VIVI	44.479933	4.691403	119	0.561	1.518

**Table S4** Seismic stations used in the study, their location, and manually picked phase arrivals. The arrival times are relative to 2019-11-23 22:14:55 UTC. This table is available in CSV format as a separate supplement, and from the code repository (see acknowledgements in the main text).

## References

Causse, M., Cornou, C., Maufroy, E., Grasso, J.-R., Baillet, L., and El Haber, E. Exceptional Ground Motion during the Shallow Mw 4.9 2019 Le Teil Earthquake, France. *Communications Earth & Environment*, 2(1):14, Jan. 2021. doi: 10.1038/s43247-020-00089-0.

Delouis, B., Oral, E., Menager, M., Ampuero, J.-P., Guilhem Trilla, A., Régnier, M., and Deschamps, A. Constraining the Point Source Parameters of the 11 November 2019 Mw 4.9 Le Teil Earthquake Using Multiple Relocation Approaches, First Motion and Full Waveform Inversions. *Comptes Rendus. Géoscience*, 353(S1): 493–516, Jan. 2022. doi: 10.5802/crgeos.78.